https://doi.org/10.5194/essd-2022-473
Preprint. Discussion started: 8 February 2023

Open Access Earth System Science Data Discussions

Glacier-level and gridded mass change in the source rivers in the eastern Tibetan Plateau (ETPR) from 1970s to 2000

Yu Zhu[1,2], Shiyin Liu[1,2*], Junfeng Wei[3], Kunpeng Wu[1,2], Tobias Bolch[4], Junli Xu[5], Wanqin Guo[6], Zongli Jiang[3], Fuming Xie[1,2], Ying Yi[1,2], Donghui Shangguan[6], Xiaojun Yao[7], Zhen Zhang[8]

1 Yunnan Key Laboratory of International Rivers and Transboundary Eco-Security, Yunnan University, Kunming 650500, China
2 Institute of International Rivers and Eco-security, Yunnan University, Kunming, Yunnan 650500, China
3 School of Resource Environment and Safety Engineering, Hunan University of Science and Technology, Xiangtan, China
4 School of Geography and Sustainable Development, University of St Andrews, St Andrews KY19 9AL, Scotland, United Kingdom
5 Department of Surveying and Mapping, Yancheng Teachers University, Yancheng, 224002, China
6 Northwest Institute of Eco-Environment and Resources, Chinese Academy of Sciences, Lanzhou 730000, China
7 College of Geography and Environmental Sciences, Northwest Normal University, Lanzhou 730070, China
8 School of Geomatics, Anhui University of Science and Technology, Huainan 232001, China

*Correspondence: Shiyin Liu (shiyin.liu@ynu.edu.cn)

Abstract. The highly glacierised eastern part of the Tibetan Plateau is the key source region of the five major rivers Yangtze, Yellow, Lancang-Mekong, Nu-Salween and Brahmaputra rivers. These exotic rivers are vital freshwater resources for more than one billion people downstream for their daily life, irrigation, industrial use, and hydropower. However, the glaciers have been receding during the last decades and are projected to further decline which will profoundly impact the water availability of these larger river systems. Although few studies have investigated glacier mass changes in these river basins since the 1970s, they are site and temporal specific and limited by data availability. Hence, knowledge of glacier mass changes is especially lacking for years prior to 2000. We therefore applied digital elevation models (DEMs) derived from large scale topographic maps based on aerial photogrammetry from the 1970s and 1980s and compared them to the SRTM DEM to provide a complete picture of mass change of glaciers in the region. The mass changes are presented on individual glacier bases with a resolution of 30 m and the grided (0.1° and 0.5°). Our database consists of 17444 glaciers with a total area of 17426 ± 523 km^2. The annual mean mass loss of glaciers is -0.28 ± 0.15 m w.e. in the whole region. This is larger than the previous site-specific findings, the surface thinning increases on average from west to east along the Himalayas-Hengduan mountains with the largest thinning in the Salween basin. Comparisons between the topographic map-based DEMs and DEMs generated based on Hexagon KH-9 metric camera data for parts in the Himalayas demonstrate that our dataset provides a robust estimation of glacier mass changes. However, the uncertainty is high in high altitudes due to the saturation of aerial photos over low contrast areas like snow surface on a steep terrain. The dataset is well suited for supporting more detailed climatical and hydrological analyses and are available at https://doi.org/10.11888/Cryos.tpdc.272884 (Liu et al., 2022).

Keywords: Glaciers; Mass change; Topo DEM

1 Introduction

Glaciers are important sources of fresh water impacting most of rivers and lakes in the High Mountain Asia (HMA) (Immerzeel et al., 2020; Immerzeel et al., 2013). They are highly sensitive to temperature and precipitation changes

https://doi.org/10.5194/essd-2022-473
Preprint. Discussion started: 8 February 2023

(e.g., Harrison (2013); Wu et al. (2018)). Due to climate change, most glaciers in HMA are losing mass with an accelerated rate during the last decades (Bolch et al., 2012; Bolch, 2019; Bhattacharya et al., 2021; Hugonnet et al., 2021; Shean et al., 2020). However, there is a great heterogeneity in mass changes with the most severe mass loss in the south and southeast part of the Tibetan Plateau compared to balanced conditions in the Karakorum and Western Kunlun Shan (Kääb et al., 2015; Shean et al., 2020).

The Yangtze, the Yellow, the Lancang-mekong, the Salween (Nu Chiang), the Irrawaddy, the Ganges, and the Brahmaputra rivers origination from the eastern and southern Tibetan Plateau and the Himalaya (here defined these regions as generalized eastern Tibetan Plateau regions (ETPR) including eastern Tibetan Plateau and regions on its south part to reduce more descriptions on the regions in results analysis and discussions), providing a significant contribution to the water supply of millions of people (Table 1), are important large rivers rise in the HMA (Fig. 1) (Immerzeel et al., 2010). There are more than 23000 glaciers (with an area of 22782 ± 683 km^2) in the source areas of these rivers, of which meltwater supply the rivers in combination with precipitation (Pfeffer et al., 2014). Snowfall, mostly taking place in Winter and Spring provided by the westerlies and during summer from the Indian and south-east Asian Monsoon, is the main accumulation source of the glaciers (Bolch et al., 2012). Most glaciers int this region are more sensitive to temperature when ice is at pressure-melting point, which results in a high ablation rates (Shi et al., 1988). In the area with annual precipitation more than 2000 mm (e.g. Kangri Karpo Mountains), a high accumulation may be presented during monsoon at meanwhile (Wu et al., 2018). Earlier studies have addressed that the glaciers suffered a substantial and increasing reduction in area, length and thickness in these areas during last three decades (e.g., Zhang et al. (2012); Xu et al. (2018); Liu et al. (2019); Wu et al. (2020)), and the loss is aggravating with the temperature rise, in combination with the differential ablation rate due to different weather conditions (Table 1), diverse topography (Hewitt, 2011), distribution of surface and surrounding features(i.e., debris, ponds, ice crevasse, proglacial lakes, etc.)(Scherler et al., 2011; Watson et al., 2018; King et al., 2019), glacier dynamics (Dehecq et al., 2018), which together poses a great challenge to evaluate and understand the glacier meltwater.

The mass balance derived from the differencing of digital elevation models is an effective approach to assess glacier mass balance (e.g. Bamber and Rivera (2007)). Recent researches based on remote sensing data have made substantial advances on quantify glacier mass change after 2000 and some extended study duration to 1970s for several regions over high mountain Asia by using the released spy satellite data and topographic maps (Maurer et al., 2019; Ye et al., 2015). However, there are evident inconsistencies due to different dataset source (Shean et al., 2020; Hugonnet et al., 2021; Zhao et al., 2022), and most of glaciers are left out because of lack of effective data, extremely before 2000. Missing data in some glacial regions before 2000 put a challenge to robustly and comprehensively quantify the sensitivity of the glaciers to climate change for a long period. Moreover, the DEMs before 2000 (i.e., KH-9 Hexagon DEMs) contain a certain amount of uncertainties due to a large number of data voids in accumulation zones of glaciers(Bhattacharya et al., 2021; Zhou et al., 2018), which make it hardly give an accurate assessment of glaciers' contribution to sea level and water demands in the downstream area. Additionally, there is less gridded product serving the energy balance simulation and the hydrological simulation in a large glacierized basin in the ETPR before 2000. We therefore aim to (1) generate a set of glacier-level and grided mass balance dataset from 1970s to 2000 based on the historical topographic maps (hereafter Topo maps) and the SRTM DEM; (2) provide a comprehensive view on the mass budget in the source area of the ETPR.

Table 1. Characteristics of the southwestern river basins. Glacier areas are based on RGI 6.0; precipitation and air temperature based on Climatic Research Unit (CRU) (average from 1970 - 2000); population (2000) are based on the GPWv4 dataset; Irrigated areas (2000) are reproduced from Siebert et al. (2015). Upstream is defined as the region with elevation higher than 2000 m.

https://doi.org/10.5194/essd-2022-473
Preprint. Discussion started: 8 February 2023

Open Access Earth System Science Data Discussions

	Ganges	Brahmaputra	Yangtze	Yellow	Mekong	Salween	Irrawaddy
Total area (km^2)	952500	629551	1920292	963345	773231	265761	375475
Upstream area (km^2)	137046	374032	628021	353312	115936	126639	29373
Glacier area (km^2)	8019.78	10411.96	2109.56	212.52	214.66	1751.92	61.71
Average temperature (°C)	21.38	10.67	11.50	5.88	21.19	11.47	21.37
Annual precipitation (mm)	1063	1560	983	367	1453	986	1775
Total Population (10^3)	391326	118716	465404	119516	48960	8155	27845
Irrigated area (km2)	275867	42363	168500	59239	24313	2043	11829

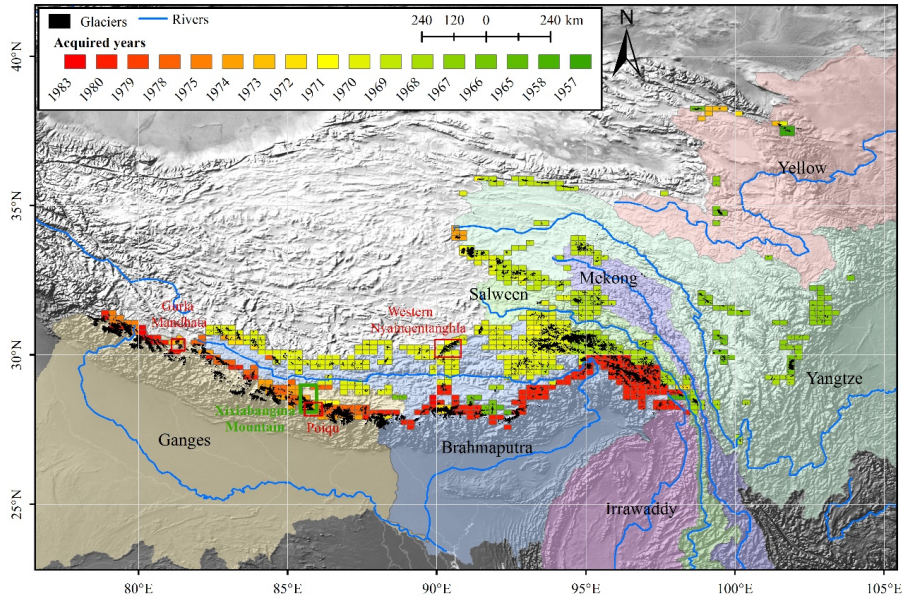

Figure 1. Glaciers in the source areas of ETPR and coverage of the Topographic maps which were generated from aerial photos acquired in various years between 1957 and 1983.

2 Data and methods

2.1 Topographic maps

We employed a total of 718 historical topographic maps including 142 at a scale of 1:50,000 and 576 at a scale of 1:100,000 compiled from aerial photos taken from 1957 to 1983 by the Chinese Military Geodetic Service (Fig. 1). These maps were presented at a geodetic reference of 1954 Beijing Geodetic Coordinate System which have a datum level based on the Yellow Sea mean sea level observed at Qingdao Tidal Observatory in 1956. Based on the National Photogrametrical Standard of China (NPSC, GB/T 12343.1-2008), the vertical accuracy is less than 5 m on slopes less than 6° and 5−8 m on slopes between 6°−25°. By using a Helmert transformation (also known as a seven-parameter transformation method), all scanned maps were rectified based on gridded points of the meridians and wefts and the geometry accuracy is controlled by over 600 ground control points measured by the State Bureau of Surveying and Mapping during 1950 to 1990, then the contours and other layers were manually digitised on-screen with the 1954 Beijing coordinate system.The These digital maps were later transformed into the coordinate system of SRTM (Shuttle Radar Topography Mission), namely the World Geodetic System 1984 (WGS84) / Earth Gravity Model 1996 (EGM96). To generate the digital elevation model (DEM), the digital contours were first used to build

https://doi.org/10.5194/essd-2022-473
Preprint. Discussion started: 8 February 2023

Triangulated Irregular Networks (TINs), and then the TINs were transformed to grided elevation products with the natural neighbour smoothing and interpolation method. The topographic DEMs (hereafter Topo DEM) were finally resampled to a resolution of 30 m to be matched with SRTM DEM. The accuracy and uncertainties of these Topo DEMs might originate from the proficiency of professionals who generated the maps using analytical plotters and aerial photo pairs, the low contrast on the areas with snow cover or cast shadows which leads to low accuracy of elevation contours, and horizontal positioning error. We will discuss these uncertainties in Section 4.1.

Based on the historical topographic maps, the first glacier inventory of China (CGI1) was compiled by a large number of experienced technician to display the status of glacier before 2000(Shi, 2008). Limited by poor technique skill and insufficient high-resolution satellite images, the first version contains a certain amount of uncertainty. To improve the accuracy of CGI1, the work group of the second glacier inventory of China (CGI2) evaluated and refined the glacier outlines in the first version of CGI1 with the technology used in processing of CGI2. The revised CGI1 was used for processing the elevation difference in this study.

2.2 SRTM

The SRTM mission provides C- and X-band topographic data in February 2000 with a 1 and 3 arc second special resolution (Farr et al., 2007). The previous studies have pointed out that the accuracy of SRTM DEM (C-band) presented a high level (-5.61 ± 15.68 m) for high relief (Carabajal and Harding, 2006). In glacierized regions, the elevation bias can be up to 10 m at high altitudes (Berthier et al., 2006). In this study, we use SRTM version 3 void-filled DEM with a resolution of 1 arc second (~30 m) refer to the glacier surface in the balance year of 1999 suggested by previous studies (e.g., Gardelle et al. (2013) and Wu et al. (2018)). In addition, the limited X-band based DEM data (Hoffmann and Walter, 2006) have been employed to quantify the underestimation of elevations in C-based DEM caused by penetration of microwaves. All datasets are downloaded from http://earthexplorer.usgs.gov/.

2.3 KH-9 data and ICESat-2 data

The ICESat-2, launched in 2018, is the second spaceborne laser altimetry mission which aims to estimate the ice sheet mass change, lake volume, and global vegetation heights (Markus et al., 2017). Similar to ICESat-1, ICESat-2 acquires the distance between the senor and Earth's surface by recording the travel time of the laser pulses, which are sent out by the Advanced Topographic Laser Altimetry System (ATLAS)— a photon-counting, 532 nm (green light) lidar operating at 10kHz. The system split the laser pulse into six beams forming 3 pairs (a weak and a strong beam separated by 90m, included in one pair) to make an accurate measurement of surface height. It takes 91 days to complete a full orbital cycle (1,387 unique reference ground tracks) (Smith et al., 2019). A ~17 m ground-footprint in diameter and ~0.7 m offset along-track for each beam makes ICESat-2 has denser footprints compared to ICESat-1. The photon geolocation information is aggregated at 40 m along-track length scales. The KH-9 images, declassified in 2002, were acquired by a cold war–era spy satellites with a flight height of approximately 170 km from 1971 to 1986. To generate a quality DEM, reseau grids overlaid on the KH-9 images was used to reconstruct the original geometry at first (Pieczonka et al., 2013). The surrounding pixels then were used to fill in the grid area and histogram equalization and Wallis filtering were applied to enhance the images. 26 evenly distributed GCPs were selected from the reference images (Landsat ETM+ images for horizonal orientation and SRTM for vertical orientation) to correct the external orientation of the KH-9 images. Several tie points in glacier regions were added manually to improve the matching accuracy and finally we got an RMSE of triangulation of 0.57 pixels. By considering the focal length (12 inches for 1973-1980), flight height, and the film size (~ 9×18 inches), the DEMs were finally generated. In some case (e.g., Bhattacharya et al. (2021)), a physical model was used to compensate the unclassified (or unknown) imaging parameters (e.g., lens distortion). These two datasets were used to evaluated

https://doi.org/10.5194/essd-2022-473
Preprint. Discussion started: 8 February 2023

the performance of elevation difference derived from the Topo DEMs.

2.4 Co-registration of TOPO- to SRTM DEMs

2.4.1 DEM co-registration and outliers processing

There are both horizonal and vertical offsets in the co-registered two DEMs due to dataset sources and the method used in production of DEMs (Paul, 2008). These offsets can be removed by using an iterative co-registration method implemented by Nuth and Kääb (2011). In this method, the elevation difference in a static off-glacier surface between two DEMs (defined as dh) were correlated with the slope and aspect of the surface (Nuth and Kääb, 2011; Berthier et al., 2007). The relationship can be quantified by the Equation (1).

$$dh = a * cos(b - \varphi) * tan(\alpha) + \overline{dh} \quad (1)$$

Where φ is aspect; α is slope; $\overline{dh}$ is the vertical offset of the registered DEM; a and b represent the horizonal offset and direction, respectively. Divided both sides of the equation by the $tan(\alpha)$, the Equation (1) can be transferred to Equation (2). The offset in x-y-z-planes (x_{off} and y_{off} are horizonal offsets; z_{off} is vertical offset) then can be represented by Equation (3).

$$\frac{dh}{\tan(\alpha)} = a * cos(b - \varphi) + c \quad (2)$$

$$\begin{cases} x_{off} = a * \sin(b) \\ y_{off} = a * \cos(b) \\ z_{off} = c * \tan(\alpha) \end{cases} \quad (3)$$

In the current study, we defined the SRTM DEM as reference DEM. The off-glacier region was identified as static surface which was assumed no elevation changes during the study period (1970s - 2000). It should be noted that the processes for registration and correction of TOPO DEM were applied in a "group-scale" rather than map-scale. Every group including at least one TOPO DEM should cover all glaciers in an independent mountain range. This was done to avoid errors resulting from the glaciers cutting by map sheet. There are total 261 groups in the ETPR. By conducting the co-registration, the resulting horizontal translation was applied to each TOPO DEM and the median vertical bias was removed. Subsequently, an elevation dependent bias due to the uneven spatial distribution of the GCPs or the low vertical accuracy of individual map were corrected by using 3-rd polynomial method suggested by the previous studies (e.g., Kääb (2008); Nuth and Kääb (2011); Pieczonka et al. (2013); Zhou et al. (2018)). Biases caused by different spatial resolutions between the DEMs could be adjusted by the relationship between elevation differences and maximum curvatures (Gardelle et al., 2013). From the histogram statistics (Fig. 2), there were three types bias of elevation differences (underestimation, low concentration, and overestimation) in off-glaciers and the corresponding corrected differences concentrated on the mean differences (tend to 0), indicating that the corrections can effectively ensure the accuracy of the elevation differences in the glacier area. After all corrections, there was a clear improvement in standard deviation (Table A1).

The corrected elevation changes with values exceeding ±150 m were assumed to be obvious outliers and removed (Bhattacharya et al., 2021; Pieczonka and Bolch, 2015). There were still some unrealistic phenomena, such as large surface thinning in accumulation zones, which are typical for Hexagon KH-9 based elevation changes (Zhou et al., 2018). These outliers were attributed to inaccurate matching of DEMs and can be removed by using an elevation dependent sigmoid function (Eq. 4) (Zhou et al., 2018; Pieczonka and Bolch, 2015).

$$\Delta dh_{max} = \left(\frac{h_{max} - h_{gla}}{h_{max} - h_{min}}\right)^2 * A \quad (4)$$

Where, Δdh_{max} represents the maximum elevation change, h_{max}, h_{min}, and h_{gla} are maximum, minimum, and pixel-level elevation respectively, and A is the maximum elevation change at a glacier's front (here we took the area 150 m from the front in statistics). We conducted the function in glacier level to avoid large elevation ranges in a

https://doi.org/10.5194/essd-2022-473
Preprint. Discussion started: 8 February 2023

specific group. The data gaps after the outlier elimination were filled using a gaussian weighted interpolation approach. In order to reduce the error propagation, we filled the data holes where area more than 0.5 km^2 by using the original values.

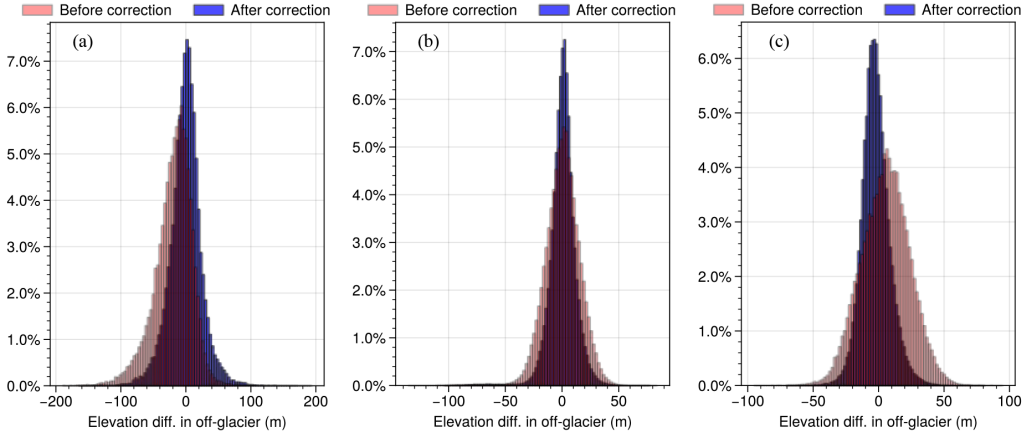

Figure 2 Elevation differences in off-glaciers of three different groups before and after registration and bias correction. (a), (b), and (c) donates representative groups with underestimation, low-concentration, and overestimation of elevation difference, respectively. The vertical axes in all subplots represent ratio of pixels in each elevation zone to total pixels.

2.4.2 Penetration depth estimation of SRTM DEM

DEMs derived from SRTM C-band contain biases due to the penetration of microwaves on dry snow, firn, and ice (Rignot et al., 2001). Since the narrow swath widths and limited available data (See Fig. A1), it is hardly to use X-band based DEM which was proved has little penetration error (e.g. Hoffmann and Walter (2006); Dehecq et al. (2016)) to calculate elevation difference. We therefore used the X-band DEM to evaluate the penetration effect of C-band DEM. Due to the elevation dependency of distribution of snow, we remove the penetration depth difference on glaciers individually in each 100 m altitude zone. The penetration depth was estimated from the off-glacier region (Fig. 3) and presented a mean of 3.8 - 6.2 m along the altitude. Note that despite penetration depth increases with increasing radar wavelength (Curlander and Mcdonough, 1991), it doesn't mean that the X-band DEM has no penetration effect. We noticed that some negative penetrations displayed in the statistics, which were regarded as the X-band penetration effects (Dehecq et al., 2016) involved in the calculation and these values were consequently removed.

https://doi.org/10.5194/essd-2022-473
Preprint. Discussion started: 8 February 2023

Open Access Earth System Science Data Discussions

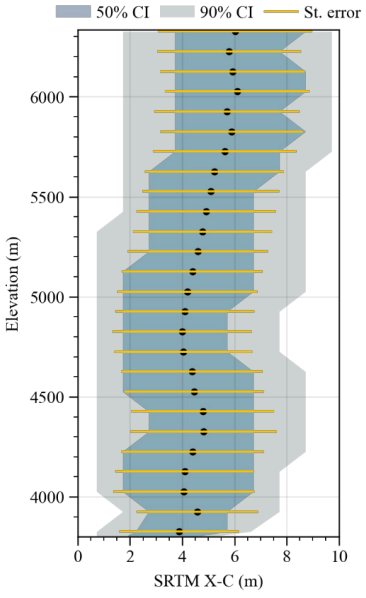

Figure 3 Distribution of the penetration depth along elevation.

2.5 Evaluation of Topo DEM based elevation difference

In theory, the reliability of the Topo DEM can be ensured by scanning maps, adjusting distortions, and generating DEM with a process approach similar to KH-9, but this is impracticable since the Topo maps are highly confidential and unavailable. Therefore, an alternative scheme is to evaluate Topo DEM by comparing its performance with a DEM based on KH-9 data acquired at approximately same time.

Topographical elevation difference accounting for the glacier thickness change is a result of the assumption that the glacier and its surrounding ground stay stable for several decades and the vertical change in glacier is totally caused by the glacier mass budget due to climate change (Hoelzle et al., 2003; Zemp et al., 2013). Thus, the performances of elevation change in the off-glacier region dominate the accuracy the glacier mass balance. KH-9 DEMs have been successfully applied to generate and analyze glacier mass balance in regional scale (e.g., Zhou et al. (2018); King et al. (2019); Bhattacharya et al. (2021)) and are thus suitable to assess the effectivity of the Topo DEM based elevation difference. The experiments were taken in the Xixiabangma Mountain range where the Topo DEM and KH-9 imagery have almost same acquisition time (Nov. 1974) and the large topographical relief can be considered as representative for the ETPR. To avoid the interference of the errors in extracting elevation difference, the same processing schemes (described in Section 2.4) except for the method of DEM generation were applied. Approximately 2800000 off-glacial pixels were involved in statistics (cf. Fig. 4a, b). Obviously, both of the differences show a similar pattern below 6000 m a.s.l.. Despite the differences in high elevation (above 6000 m a.s.l) presented partly different performances (negative difference for Topo and positive difference for KH-9 in the elevation ranges of 6000 – 7000 m a.s.l.), the large standard deviation (more than 40m) of two differences indicated a fact of low reliability of elevation difference in the high altitude. In order to quantitatively evaluate this similarity, we implemented histogram statistics, in which the mean and standard deviation in off-glacial elevation difference before and after the correction procedure were calculated. It is distinct that the elevation difference of the Topo DEM displayed a more concentrated distribution centred around 0 than that of KH-9 DEM (Fig. 4e and 4f). The

https://doi.org/10.5194/essd-2022-473
Preprint. Discussion started: 8 February 2023

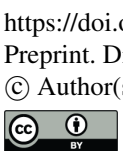

Open Access Earth System Science Data Discussions

surface-elevation change error of KH-9 and Topo DEM is 1.57 and 0.31 respectively, which indicates that the Topo difference manifests a superior expression in glacier mass balance than KH-9.

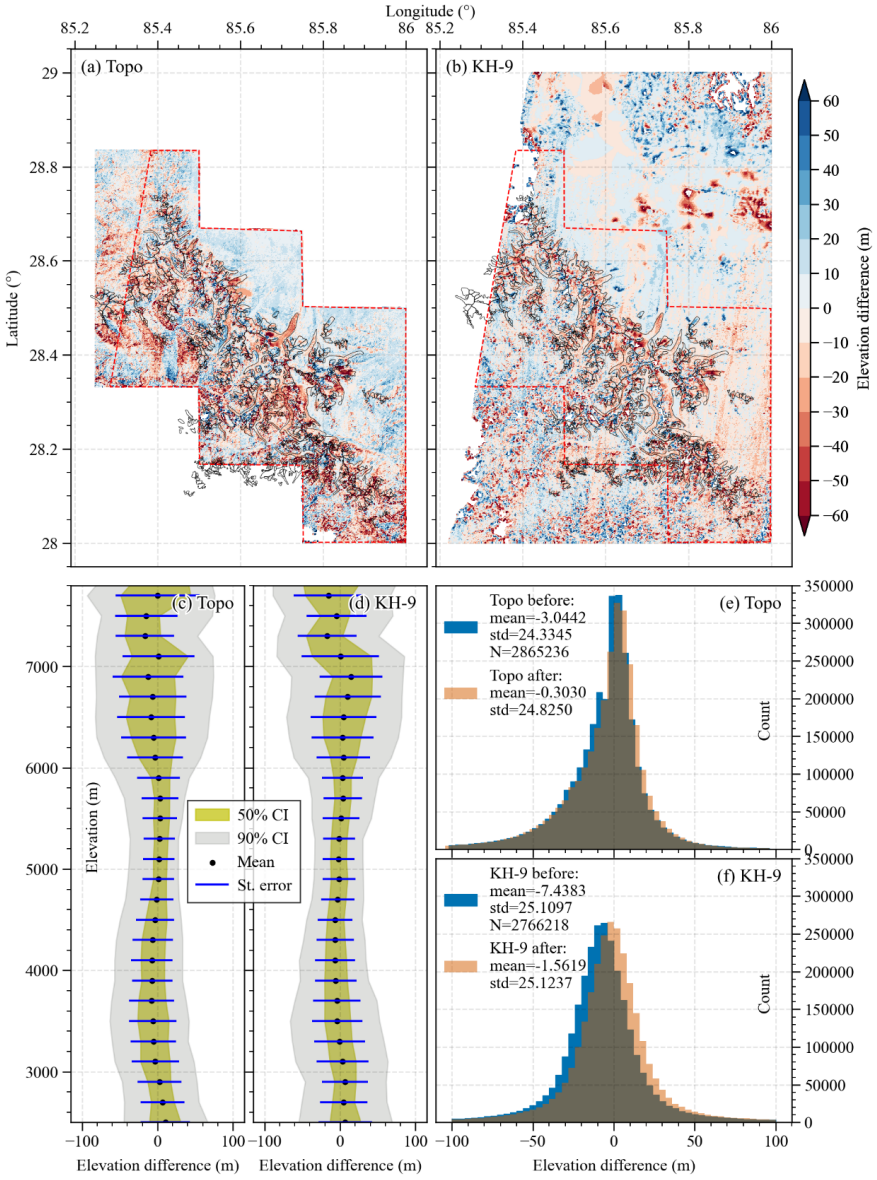

245 **Figure 4** Comparation of (a) Topo based and (b) KH-9 based elevation difference at the off-glacier region. The statistics on elevation difference along elevation for Topo and KH-9 results were displayed in (c) and (d). (e) and (f) show frequency of Topo based and KH-9 based elevation difference. The CI denotes the confidence interval.

In addition, we perform a further evaluation of the Topo DEM by comparing ICESat-2 ATL06 along track

https://doi.org/10.5194/essd-2022-473
Preprint. Discussion started: 8 February 2023

heights (time range from Oct. 2018 to Feb. 2019) to the stable (off glacier) area of the Topo DEM. The ATL06 products represent the mean surface elevation with a horizontal accuracy of less than 10 m and a vertical accuracy of within 3 mm (Smith et al., 2020; Brunt et al., 2019). Despite the mean elevation differences from ATL06-SRTM and SRTM-Topo below 5700m are close to 0, the values of ATL06 display a more discrete distribution in a specific altitude zone (Fig. 5b). This probably attributes to matching error between the laser points and SRTM since the accuracy of SRTM is limited by a 30 m resolution. We thus find that the accuracy of corrected Topo difference is not less accurate than the ATL06 difference below 5700 m. For the high elevations, the negative differences can be related different snow thicknesses both based on seasonal snowfall and atmospheric warming. The large changes in the off-glacier region leads to an issue that we cannot evaluate the reliability of the Topo DEM via ATL06 at high altitude. Despite the Topo DEM performed a high agreement with other elevation data derived from different sensors and generated by different methods, the uncertainty in high elevation (above ~5700 m) is a critical limitation to the elevation differences in the accumulation zone of glacier. Nevertheless, this is a common issue for the DEM derived from historical optical images (e.g., Zhou et al. (2018)) and can hardly be improved since low accuracy of photographing equipment, a lack of GCPs, the seasonal variance due to random shooting time, etc. We therefore did not target this in the current dataset and just estimated the errors in glacier surface elevation changes based on the differences in corresponding off-glacier area.

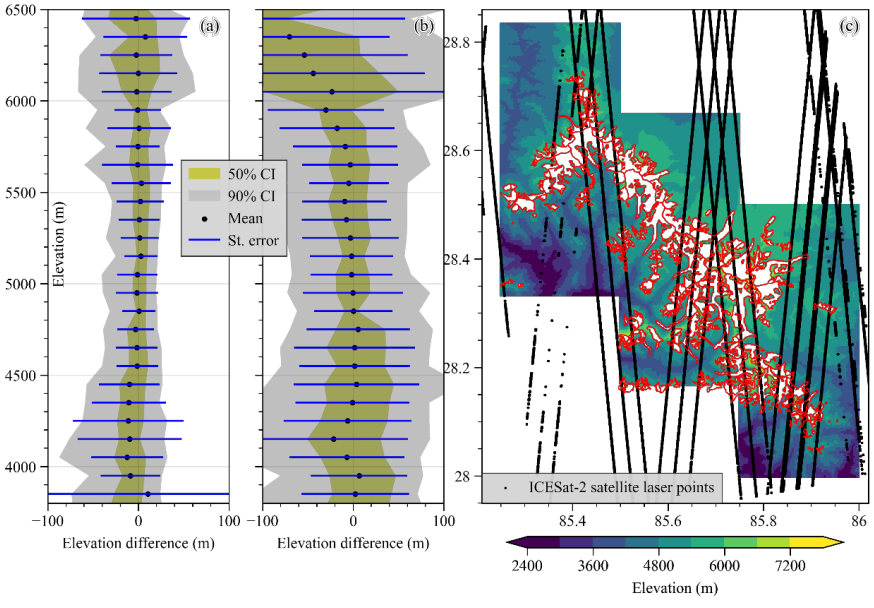

Figure 5 Performance of (a) the Topo DEM and (b) ATL06 heights with elevation in the Xixiabangma Mountain range. (c) Tracks of ATL06 are. The elevation zones with laser spots less than 200 were not included in the statistics.

2.6 Uncertainty estimation

The annual surface elevation changes ($\frac{\partial dh}{\partial t}$) were converted to mass changes (M) by using the equation 5. A standard bulk density of ρ=850 kg m^{-3} (Huss, 2013) was applied to assess the water equivalent.

$$M = \frac{\partial dh}{\partial t} * \rho \quad (5)$$

https://doi.org/10.5194/essd-2022-473
Preprint. Discussion started: 8 February 2023

To adapt the application in hydrology, we imposed glacier polygons of revised CGI1 rather than the minimum glacier area threshold. For the potential studies using this dataset, we also provide the elevation difference and corresponding attributions (e.g., the uncertainties and the acquisition time for the Topo maps) so that the potential users can define the ρ and the minimum glacier polygons and get the mass balance as their purpose.

We employed the similar approaches to estimate the uncertainty in glacier mass balance (e.g., Berthier et al. (2016); Wu et al. (2018); Shean et al. (2020)). The biggest uncertainty in mass balance contains in elevation changes (σdh). To estimate it, we calculated statistics of elevation differences for off-glacier regions, assuming that elevation changes should be close to 0. Firstly, we calculated the mean elevation differences (MED) to quantify the systematical uncertainties in elevation difference. Then, the standard deviation (SD) of the mean (SDE) was applied to measure the spread of the uncertainty (random error) (Wu et al., 2018). A decorrelation length scale of 600 m was applied in the calculation of the random error to reduce to autocorrelation of the elevation difference (e.g., Bolch et al. (2011)). The final uncertainty for the elevation change was estimated by calculating total root-mean-square error (RMSE) with MED and SE (Equation (6)). It should be mentioned that the uncertainty involved in the radar penetration depth recovery will also affect the elevation change estimation since there can be few meters of penetration of the X-band radar into dry snow (Dehecq et al., 2016), but this usually be ignored for an over ten years period, unless evaluating annual cycle of mass balance.

$$\sigma dh = \sqrt{MED^2 + SE^2} \quad (6)$$

Where $SE = SD/\sqrt{N}$ and N is the number of the pixels involved in statistics.

The uncertainties included in the glacier area and glacier density should be taken into account in the estimation of the mass balance uncertainty. The uncertainty of glacier area is reported approximately 8% for the South Asia (Pfeffer et al., 2014), the uncertainty of glacier area therefore can be assumed 10% (0.1·glacier area A) (e.g., Kääb et al. (2012); Shean et al. (2020)) to account for temporal evolution of glacier extent and glacier boundary mapping. Referring to study of Huss (2013), the density uncertainty can be assumed to $\Delta\rho$=60 kg m^{-3}. We assumed that all of these uncertainties are uncorrelated, so the total uncertainty in mass balance can be estimated by Equation (7) (Pieczonka and Bolch, 2015).

$$\sigma M = \sqrt{\left(\frac{dh}{t} * \frac{\Delta\rho}{\rho_w}\right)^2 + \left(\frac{\sqrt{\sigma dh^2 + \left(\frac{\sigma A}{A}\right)^2}}{t} * \frac{\rho_i}{\rho_w}\right)^2} \quad (7)$$

Where, dh glacier thickness change, t donates the observation period, σA and $\sigma\rho$ are glacier area uncertainty and density uncertainty, respectively. In addition, the uncertainty involved in the resampling of grided products were estimated by SE in grid scale.

The statistical uncertainties display a regional difference and the Irrawaddy shows the largest error, followed by Mekong (Table 2). Since the processing was implemented in the group-scale, glaciers in a specific group displayed a same error (See the attributes of the dataset). The uncertainties of grided products which include the elevation difference uncertainties and resample uncertainties were shown in the Fig. A3 and also can be found in the grided dataset.

Table 2 Statistics of vertical errors in each basin

Region	MED(m)	SD(m)	N	No. of Group	SE(m)	σdh(m)
Ganges	-0.639	32.000	22547860	17	0.028	0.639
Brahmaputra	-0.303	22.839	138764282	147	0.024	0.303
Salween	-0.355	22.908	17714420	26	0.029	0.356
Mekong	-0.746	17.171	4157616	5	0.019	0.746

https://doi.org/10.5194/essd-2022-473
Preprint. Discussion started: 8 February 2023

Yangtze	-0.399	23.413	21544718	49	0.035	0.401
Yellow	-0.135	15.256	2709178	13	0.033	0.139
Irrawaddy	-0.963	38.722	4403658	4	0.037	0.964

2.7 Glacier-level and gridded mass change dataset

Based on the final generated mass change data, mass change of each glacier was extracted to generate glacier-level products. To avoid the errors in incomplete statistics of each glacier due to the coverage of topographical maps and the outliers in the elevation difference, coverage ratios (defined as the ratio of elevation difference grid count and glacier grid count) in the accumulation zone (hereafter R_acc) and the ablation zone (hereafter R_abla) were defined to select the glaciers which have sufficient coverage of elevation difference. The accumulation and ablation zone for a specific glacier are identified by Equilibrium Line Altitude (ELA) which was defined as median surface elevation of a glacier referring to Sakai et al. (2015). We defined a glacier with R_acc ≥ 0.4 and R_abla ≥ 0.5 as an effective glacier which can be involved in the following statistics. In total, 17444 out of 23178 (~75%) glaciers met this criterion. In the glacier-level products, the uncertainties of elevation difference and grided shotting year of Topo maps were included.

Compared to the glacier-level products, the key issue for grided dataset is the representativeness of the elevation difference in each grid rather than the coverage ratios. This means that a large number of samples are required for a specific grid, especially for grid with large size (e.g., 0.1°). However, most of the studies cannot meet this requirement and mostly aim at discussing the regional mass changes or integrating the representative glacier to estimate the mass budget in a large-scale (e.g., Pieczonka and Bolch (2015); Kumar et al. (2020); Bhattacharya et al. (2021)). The sufficient coverage topographical maps ensure sufficient samples for producing the grided product. The detailed processing for these two datasets can be found in Fig. 6. We refer to A3 for the corresponding descriptions of the products.

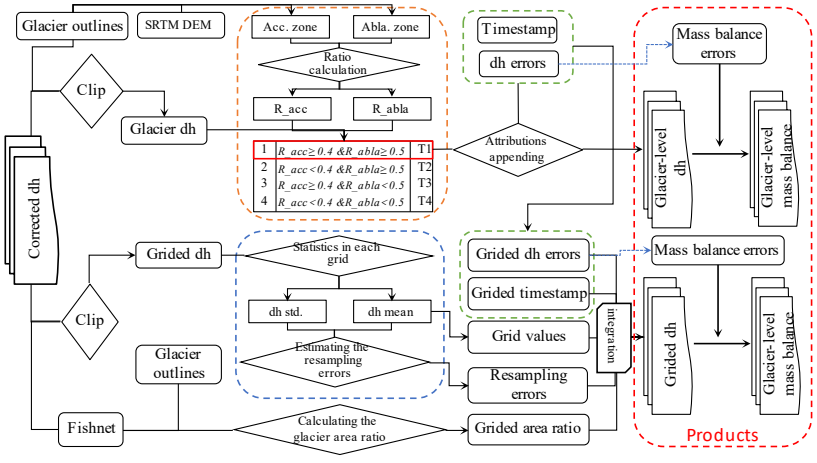

Figure 6 Diagram of the glacier-level and gridded products generation workflow.

3 Results

3.1 Glacier-level mass change

The area involved in statistics accounts for 76.5% of total glacierised area. The average elevation difference for the

https://doi.org/10.5194/essd-2022-473
Preprint. Discussion started: 8 February 2023

period from 1970s to 2000 was -9.72±5.82 m, corresponding to a mass change of -0.275±0.152 m w.e. yr^{-1}. Small glaciers showed more reduction in mass than large glaciers. The glaciers with an area less than 50 km^2 and greater than 30 km^2 displayed relatively strong thinning (Table 3). The relatively large standard deviations for large glaciers indicate that great spatial variability exists. The uncertainties in surface thickness change ranges from 0.74~2.55 m for the study period which can be found in glacier-level dataset. The large glaciers are increasingly important as they will exist for a longer time and smaller glaciers will continuously vanish due to climate change. Furthermore, we conducted the statistics on the glacier with area more than 10 km^2 to give a perspective of elevation changes in large glacier (Fig. 7). The eastward glaciers which account for the largest area proportion showed largest thickness reduction (~ -12m). Despite there were few glaciers (3%, 175.602 km^2 out of 5955.707 km^2) with an average slope less than 10°, they showed great glacier surface thinning among all slope ranges except for westwards glaciers.

The large river basins exhibited similar mass losses with values about -0.30 m w.e. yr^{-1} (Table A4). Also Ganges (-0.28 ± 0.18 m w.e. yr^{-1}) and Brahmaputra (-0.27 ± 0.12 m w.e. yr^{-1}) which contain together over 80% of the glacier coverage in ETPR showed the similar mass balances.

Table 3 The statistics of elevation difference for different glacial scale. The standard scale range for glaciers refers to Shi et al. (1988).

Area range (km^2)	No. of glaciers	Glacier area (km^2)	No. involved in statistics	Area involved in statistics (km^2)	Elevation diff. (m)	Std. (m)
≤0.5	15704	2919	11934	2215	-10.326	12.1
0.5-1	3271	2299	2383	1682	-9.618	13.8
1-5	3439	7091	2545	5298	-9.525	15.1
5-10	443	3065	330	2276	-9.227	17.1
10-30	261	4384	202	3445	-8.652	19.3
30-50	42	1601	35	1337	-9.640	23.2
50-80	12	721	10	594	-7.485	23.8
80-100	3	272	3	272	-7.399	16.6
100-300	3	430	2	308	-6.432	17.8

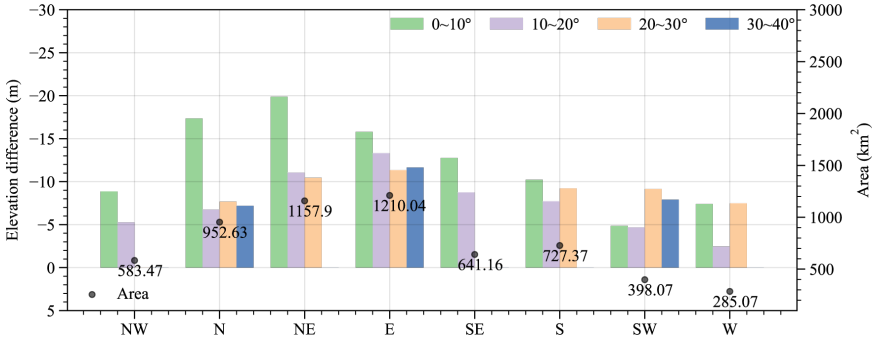

Figure 7 Elevation difference for large glaciers (> 10 km^2) depending on aspect and slope

3.2 Grided glacier mass balance

The given gridded products allow for the identification and analysis of hotspot regions and zones over the ETPR at 0.1° and 0.5° resolution. Moreover, they are import to support for description of glacier runoff in a glacierized basin and parameter calibration of a simulation of glacier meltwater contribution to total runoff by hydrology models. The glacier mass balance in the ETPR is -0.28 m w.e. yr^{-1} (equal to -9.81 m surface thinning during study period) with a 0.5° grid scale for the investigated period (Fig. 8). The different grid size leads to slight but insignificant

https://doi.org/10.5194/essd-2022-473
Preprint. Discussion started: 8 February 2023

differences in mass balance, for instance, the original product with a resolution of 30 m resulted in a -9.72 m glacier surface thinning compared to a -9.71 m observed by the 0.1° grid product. This is a result of resampling and have been provided for each product. An apparent discrepancy in mass balance is noted in the meridional and the zonal distribution, which is characterized by a decrease in mass balance with the increase of latitude except for 37°N and two hotspot regions (the source area of the Brahmaputra and the source area of the Mekong and the Salween) with largest negative mass balance along meridional direction.

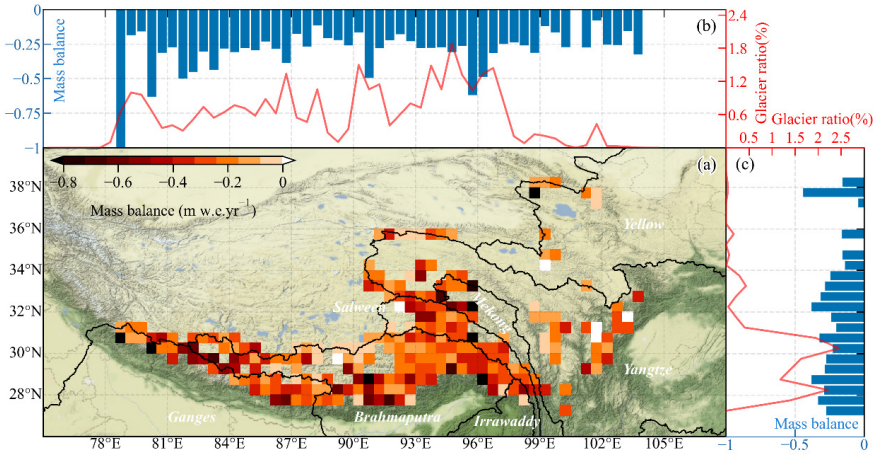

Figure 8 Characteristics of grided mass budget over the ETPR. The glacier ratio accounts for the glacier area divided by grid area.

4 Discussions

4.1 Uncertainties of the Topo DEM

By executing the co-registration with SRTM DEM, the horizontal positioning errors in the Topo DEM can be largely eliminated. However, uncertainties of the Topo DEM stem from the process of the generation of the contours and the interpolation. To obtain high accuracy of topographical maps, it is important to meet the basic intervals between contours (see Table A3). However, it is increasingly difficult in steep terrains because dense lines cannot be draw in the limited space (Fig. A4). This coupled with the strategies in cartographic generalization of diverse land cover, lead to uncertainties in the contours. We assume that these uncertainties are presented as the elevation difference in the stable terrains based on the theory of error propagation.

To assess the uncertainties, we implemented statistics for all off-glacier regions, where the land cover was divided into six kinds (Fig. 9). The grassland presents the smallest uncertainty (~ 0.31 m), followed by the bare land (~ -0.44 m). The high accuracy in grassland and bare land benefits from these two types of land cover have little extra height compared to the forest land. Besides that, the grassland and bare land display larger and more continuous plaques in high altitude regions compared to forest, which makes them be marked with more elevation points. It is obviously that there is a positive elevation difference (~1.21 m) which we concluded as the result of that the height of the trees in contour was ignored. Snow cover region shows increasingly uncertainties among the elevation rise and the increasing slope. Despite the snow cover accounts for approximately 8% of the area of the whole statistical region, its uncertainty is closely related to the uncertainty in glacial area since the similar distributions. The high density of contour lines is a guarantee of obtaining fine topographic mapping in high-altitude

https://doi.org/10.5194/essd-2022-473
Preprint. Discussion started: 8 February 2023

areas where usually have steeper terrains than the low-altitude. However, this requirement is difficult to meet in production of the topographic maps because of the limited identify capability of mapmaker. Considering that there are a few application scenarios for high altitude terrain, the drawing spacing of contour lines, in the national standard, is even lower than that in flat areas (see Fig. A4 and Table A2). This is the primary cause for the large uncertainty of elevation in high altitude zones with snow cover. The elevation deviation of snow cover area at low altitude is a result of seasonal change of snow cover, contributing little impaction to long-term glacier elevation difference. Due to dispersed distributions of water bodies and the expansion of the lakes during study period, the elevation difference in water bodies is inaccurate and cannot be used for uncertainty assessment. The uncertainties in orientation have no notable difference, which is largely due to the similar proportions of all kinds of land cover. On the whole, the uncertainties increase with slope, which may attribute to the compilation specifications, but the more important thing is the poor technical conditions at that time leading to substandard performance in the steep terrains. The slope dependency of accuracy is common with other DEM products, such as SRTM DEM, ASTAR GDEM, and SPOT5-based DEM, etc.(Kocak et al., 2004; Rodríguez et al., 2006). This means that geodetic-based ice mass changes by might have a great uncertainty in steep terrain which largely exists in the accumulation zones of glaciers.

Another uncertainty is the interpolation in generating DEM from the contours. Interpolation methods have a certain amount of influence on accuracy and natural neighbour method displays a relative high accuracy(Habib, 2021). However, all the methods cannot get satisfied results in high altitude regions since interpolation led to a smooth surface structure, especially in steep slopes. This means that the interpolation uncertainty also relates to terrain conditions. Despite the meshing procedure can be used to establish a coarser topographical structure which is more closed to real terrain (Pieczonka et al., 2011), the limited number of elevation points (8-15 for per 100 mm^2 in alpine region in topographical maps according to GB/T 12343.1-2008) makes it hard to conduct this procedure when generating Topo DEMs. Even so, there are numerous successful application research on glacier changes based on topographical maps (e.g., Ye et al. (2017), Junfeng et al. (2018), Wu et al. (2018), and etc.)

https://doi.org/10.5194/essd-2022-473
Preprint. Discussion started: 8 February 2023

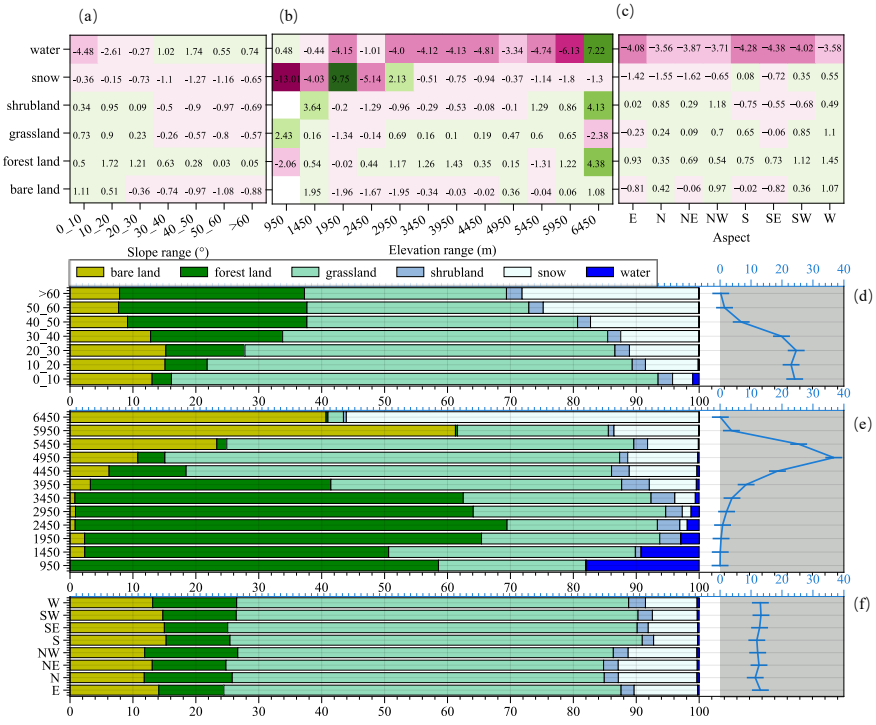

Figure 9 Characteristics of elevation difference of off-glacier in different (a) slopes (b) elevation zones, and (c) aspects on different land covers. The land cover ratios are displayed in d, e, and f. The blue lines in gray shadows in d, e, and f represent the total area proportions in a specific classification. The units in a, b, and c are m, while in d, e, and f are %.

4.2 Comparison with KH-9 based results

There, to date, is little observation for mass changes before 2000 in the whole ETPR. Few regional studies based on topographical maps (e.g., (Ye et al., 2015)) but with small coverage. A number of studies based on KH-9 (e.g.,(Maurer et al., 2019) and (Bhattacharya et al., 2021)) with sufficient coverages can be an independent source for comparison and validation of Topo DEM based mass balance.. We therefore compared our dataset with the assessments from KH-9, such as the works of Zhou et al. (2018) and Bhattacharya et al. (2021). The KH-9 based results mostly concentrated on the mass change in the Himalayas and concluded results ranging from -0.17 to -0.32 m w.e. yr^{-1} (Table A3). These results are basically consistent with ours. However, some differences in the basin scale (or regional scale) were found, for example, the Yigong Zangbo and Parlung Zangbo (mainly included in the Salween and the Brahmaputra) were reported a mass balance of -0.11 ± 0.14 m w.e. yr^{-1} and -0.19 ± 0.14 m w.e. yr^{-1}respectively by Zhou et al. (2018) compared to a mass balance less than -0.24 ± 0.13 m w.e. yr^{-1} derived from Topo DEM which is partly due to an incomplete statistics of the previous study. This difference also emphasizes the importance of data source and methodology for the evaluation of mass balance. The results of Bhattacharya et al. (2021) were used as the reference to conduct a further analysis since other datasets were not available.

Our total ETPR-wide mass balance (-0.28 m w.e. yr^{-1}) is larger than the budget (-0.22 m w.e. yr^{-1}) estimated by using the dataset of Bhattacharya et al. (2021). This difference in the mass budget may be related to differences in methodology for the generation of DEMs from optical photography. It could also be linked to the inconsistent periods for elevation difference, that is the acquisition dates for KH-9 images largely ranging from 1964-1976

https://doi.org/10.5194/essd-2022-473
Preprint. Discussion started: 8 February 2023

compared to topographical maps ranging from 1957-1983, despite the annual differences were used for comparison. However, the most important reason is the coverage of the results. Since the great topographic relief and different meteorological conditions lead to the spatial heterogeneity of glacier mass balance in a large region, even in a specific mountain range (Wang et al., 2019), it is hardly to evaluate that if the regional mass balance can be regarded as the representative of the mass budget in the large extent. Therefore, the regional comparation (regions covered by both KH-9 and Topo) can be meaningful to analyze the performance of the differences.

Due to the availability of the KH-9 elevation difference, only two sub-regions of the Ganges basin and one sub-region of the Brahmaputra basin were used. Overall, two results display the similar heterogeneity in mass changes from east (Western Nyainqentanghla) to west (Gurla Mandhata). Our result of -0.18 ± 0.06 m w.e. yr^{-1} in the Western Nyainqentanghla is on average smaller than the estimate based on the KH-9 (-0.24 ± 0.12 m w.e. yr^{-1}) during 1976-2001 (Bhattacharya et al., 2021) but they match within their uncertainty. This could be attributed to the slightly different acquisition times amongst other reasons mentioned. By comparing the elevation differences in the sub-region (Langtang) of the Poiqu (Fig. 10d and 10e), we conclude that the difference of the data-filling strategies and glacier boundary is also a trigger for less negative mass change in our results. In order to clarify this phenomenon and promote more flexible applications of our dataset, we also provide the elevation change data with no gap filling. For the Gurla Mandhata region, the more negative mass balance from Topo is mainly due to the data-filling strategies (the filled region (6250 - 6900 m) in Topo shows a negative mass budget with the value near 0, whereas the corresponding region in KH-9 shows a gap).

For all compared regions, the annual elevation differences display similar pattern along the altitude between KH-9 and Topo. However, the elevation change derived from the KH-9 DEM is more negative than that from the Topo DEM at the glacier tongue (Fig. 10c, f, and i). This difference (0.2 -0.5 m/yr) is quite large in the Nyainqentanglha region. Despite it is obvious that our result excluded small part of glacier tongue where exhibits the largest surface thinning, our results present relatively small variations (std. is 9.68) along the elevation, which is different from the distribution of the elevation difference from KH-9. This may be a result of the uncertainties in the production of the Topo DEM or KH-9 DEM.

To further confirm that our data can give a comprehensive and effective expression in the whole study region, we conducted a comparison with the results after 2000 (i.e. Brun et al. (2017), Shean et al. (2020), and Hugonnet et al. (2021)) which have a more extensive coverage. Both the results indicate that the source area of the Salween is the center of strong mass loss, which is consistent with the estimate of the Topo. However, the results derived from KH-9 indicated that the east-central Himalaya was the region with largest glacier surface thinning. Assuming that the climate condition changed in a close variability for the different basin, the mass budget will keep the same spatial heterogeneity in basin level for the study period. By comparison, the Topo-derived mass balance was found to exhibit the same spatial heterogeneity with the average of the estimates of Brun et al. (2017) and Shean et al. (2020) (the Yellow River basin and Irrawaddy River basin were excluded in the statistics since both basins have little glacier cover). This indicated that the coverage of the dataset will lead a partly different knowledge in heterogeneity of glacier mass budget.

Table 4 Glacier mass balance of the selected areas derived from KH-9 and Topo DEMs. Source of the results derived from KH-9 panoramic camera data: Bhattacharya et al. (2021)

Region	KH-9	Topo	Periods (KH-9 vs. Topo)	Referred watershed
Western Nyainqentanghla	-0.24±0.13	-0.18±0.06	1976-2001 vs. 1974-2000	Brahmaputra
Poiqu	-0.30±0.10	-0.26±0.16	1974-2004 vs. 1970-2000	Ganges (east)
Gurla Mandhata	-0.12±0.10	-0.15±0.08	1974-2004 vs. 1974-2000	Ganges (west)

https://doi.org/10.5194/essd-2022-473
Preprint. Discussion started: 8 February 2023

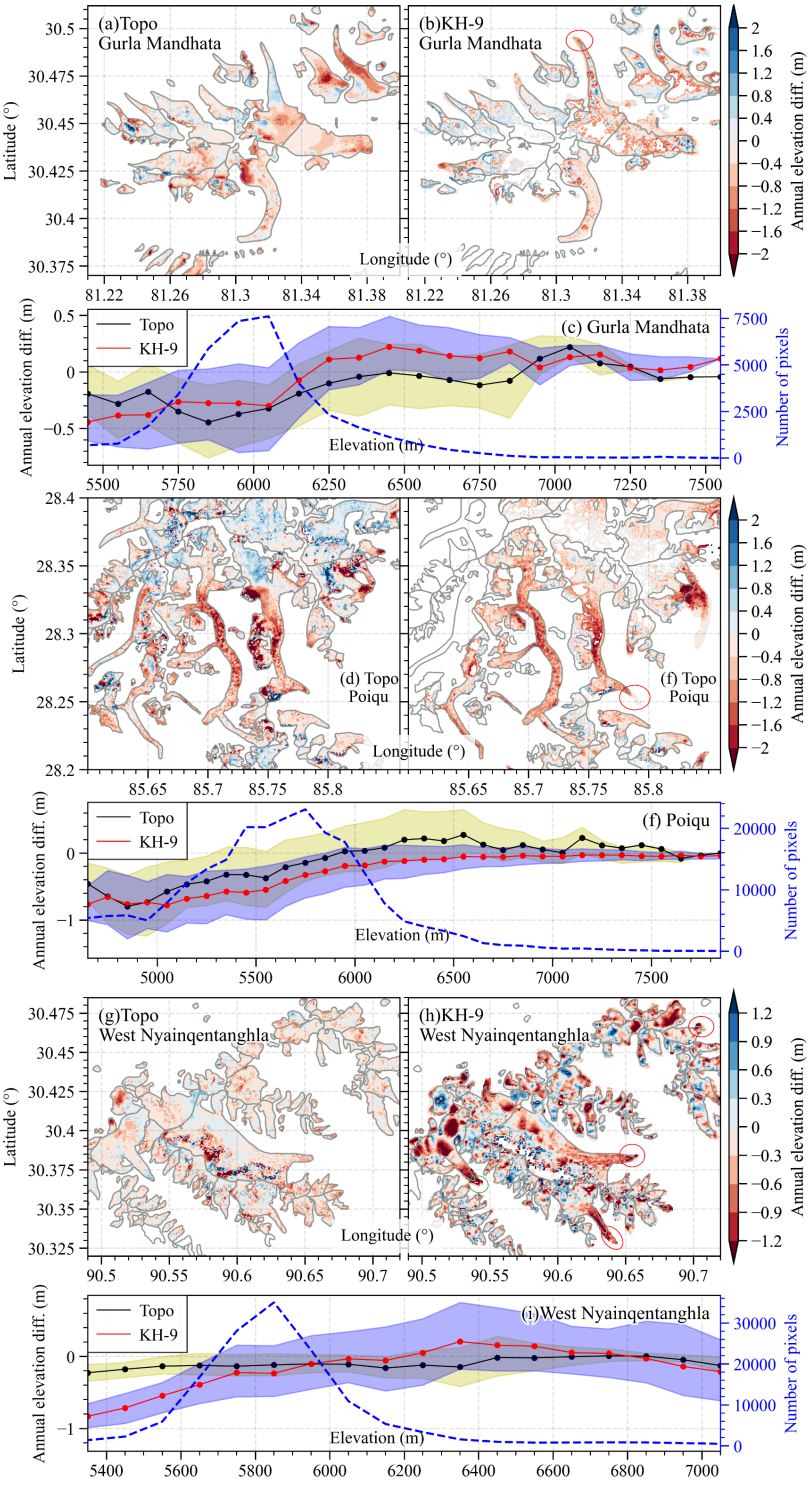

https://doi.org/10.5194/essd-2022-473
Preprint. Discussion started: 8 February 2023

Figure 10 Annual elevation difference extracted from Topo and KH-9. The distribution of elevation difference along altitude is presented in c, f, and i. The red cycle in figures mark out the noticeable difference between Topo and KH-9 caused by inconsistent the glacier outline. The light shadows in c, f, and i represent the 50% CI.

5 Conclusions

This study produced a nearly complete inventory (75% of glacier polygons) of glacier mass change dataset to provide a comprehensive view of the heterogeneity of glacier change before 2000 across the study area. The grided products, in combination with the published results, provide a nearly 5 decades mass balance to support parameter calibration in hydrological simulation and energy balance simulation, and to evaluate the contribution of mountain glacier loss to sea level.

There overall mass balance in the ETPR from 1970s to 2000 is -0.28 ± 0.15 m w.e. yr^{-1}. Small glacier experienced the most negative mass change. The mass balance has an obvious meridional characteristic that the farther east, the greater the mass loss.

The uncertainties in mass budget mainly originate from the generation process of the contours. This uncertainty increases along the slope, attributing to the compilation specifications, and the poor technical conditions, which leads to low accuracy in elevation change at steep terrain.

The systematical comparisons on Topo and KH-9 indicated that our product can at least reach the accuracy level of KH-9. However, both Topo and KH-9 based results give a low reliability at high altitude. Overall, the mass balance obtained by Topo is consistent with KH-9 based result. The knowledge on mass balance at some region is different from the findings based on KH-9, which probably due to the narrow coverage of KH-9 maps and the method adopted in generating DEM.

6 Data availability

The ETPR glacier surface mass change database is distributed under the Creative Commons Attribution 4.0 License. The data can be downloaded from the data repository of the National Tibetan Plateau/Third Pole Environment Data Center at https://doi.org/10.11888/Cryos.tpdc.272884 (Liu et al., 2022).

Appendix A

A1 Improvement for the elevation difference

Table A1 Performance of elevation difference in off-glacier in the correction process.

Basin	Std.			Mean		
	original	co-registration	3rd polynomial	original	co-registration	3rd polynomial
Yangtze	23.609	21.639	21.524	-6.205	-1.541	-0.352
Ganges	24.373	22.551	22.527	-2.189	-2.025	-0.512
Mekong	27.568	24.725	24.664	-7.169	-3.444	-0.332
Salween	24.005	22.578	22.415	-2.593	-1.450	-0.111
Brahmaputra	27.516	25.623	25.411	0.089	-1.416	-0.379
Yellow	15.907	14.881	14.862	-1.042	-0.903	0.190
Irrawaddy	35.687	33.302	33.059	3.110	-2.938	-1.209

A2 SRTM X-band images

https://doi.org/10.5194/essd-2022-473
Preprint. Discussion started: 8 February 2023

Open Access Earth System Science Data Discussions

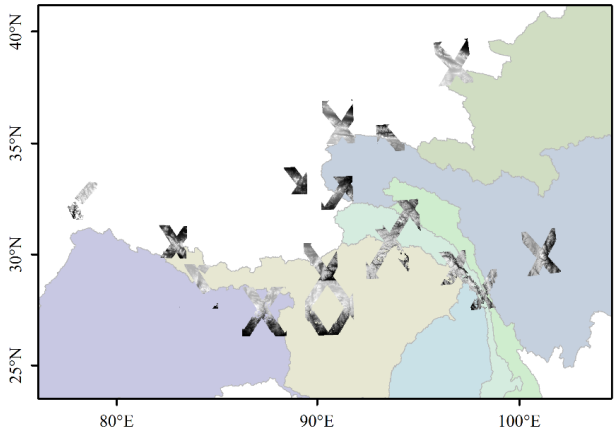

Figure A1 SRTM X-band images used in this study

A3 Descriptions of the products

The glacier-level dataset is given in a NetCDF format and has five layers (Fig. A2). The *mb* layer represents the annual mass balance during 1970s~2000 for each glacier. The *topo_dh* layer represents the elevation difference from the year given in *dxt_id* layer to 2000. The *topo_dh_fill* layer denotes the corrected elevation difference from gap filling with gaussian weighted interpolation. The *elevation* layer is the corresponding elevation derived from SRTM DEM, which can used to display the elevation difference along the elevation zone. The dataset is in a coordinate system of Albers Conic Equal Area and can be transfer to WGS84 easily by using a python package *rioxarray* (https://corteva.github.io/rioxarray/stable/). The uncertainty related statistics information is given in the attributes of *topo process group*, *topo off-glacier dh std*, *topo off-glacier dh mean,* and *topo dh error*. The projection information and resolution can be also found in the attributes and which can used to transfer the NetCDF format to the GeoTIFF format.

The Grided dataset is given in a NetCDF format and has eight layers (Fig. A3). The *mb* layer represents the annual mass balance during 1970s~2000. The *dh* layer and *dxt_year* layer represents the elevation difference and the shooting year respectively. The two error layers *dh_error* and *res_error* decide the uncertainties in mass balance (*mb_error*). The *gla_flag* layer records the status of the grid, i.e., 0 for no glacier, 1 for glacier & dh, and -1 for no covering of the Topo map. The *gla_ratio* layer denotes the ratio of glacier area to grid area. This dataset is given in the WGS 84 coordinate system in order to in consistent with the popular reanalysis dataset (e.g., ERA5).

https://doi.org/10.5194/essd-2022-473
Preprint. Discussion started: 8 February 2023

Open Access Earth System Science Data Discussions

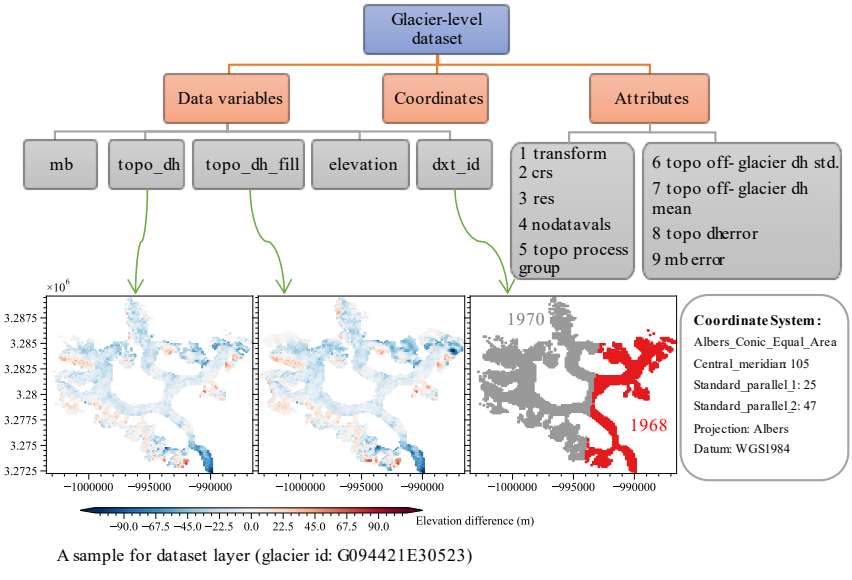

Figure A2 The structure of glacier-level dataset.

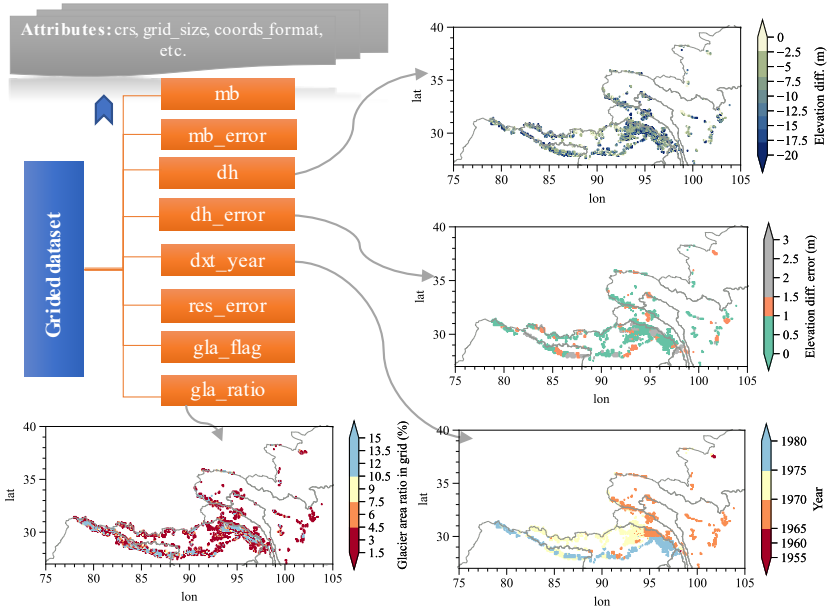

Figure A3 The structure of glacier-level dataset. The sample data is from the 0.1° production.

A4 Standards in generating Topo maps

Table A2 The standard for generating contours from aerial photos (NPSC, GB/T 12343.1-2008).

https://doi.org/10.5194/essd-2022-473
Preprint. Discussion started: 8 February 2023

Landform	Basic contour distance (m)	
	1 : 50000	1 : 100000
Flat ground (Slope < 2° & elevation difference < 80 m)	10 (5)	20 (10)
Hill area (2° ≤ Slope < 6° & 80 m ≤elevation difference < 300 m)	10	20
Mountainous region (6° ≤ Slope < 25° & 300 m ≤elevation difference < 600 m)	20	40
Alpine region (Slope > 25° & elevation difference > 600 m)	20	40

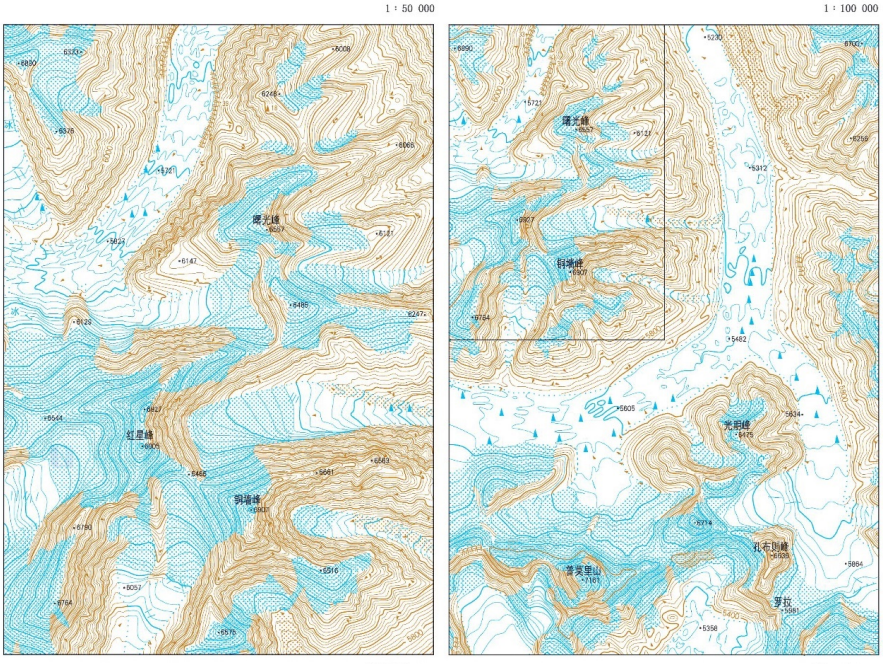

Figure A4 A sample of topographical maps in glacierized region (originate from the NPSC, GB/T 12343.1-2008).

A5 Previous studies on mass balance in ETPR

Table A3 The previous studies using 1970s KH-9 Metric Camera imagery in the study area.

Region	Mass balance (m w.e. yr^{-1})	Period	Reference
Himalayas (25° - 37°N, 75° - 93°E)	-0.22 ± 0.13	1975 - 2000	Maurer et al. (2019)
Himalayas (25° - 37°N, 75° - 93°E)	-0.25 ± 0.09	1974 - 2000	King et al. (2019)
Langtang (28.10°-28.39°N, 85.50° - 85.80°E)	-0.24 ± 0.08	1974 - 2006	Ragettli et al. (2016)
Gangotri Glacier, Garhwal (30.802°N, 79.147°E)	-0.20 ± 0.01	1968 - 2006	Bhattacharya et al. (2016)
Eastern Himalayas (27.90°- 28.35°N, 89.80° - 90.90°E)	-0.17 ± 0.05	1974 - 2006	Maurer et al. (2016)
Everest area	-0.28 ± 0.12	1962 - 2001	King et al. (2020)

https://doi.org/10.5194/essd-2022-473
Preprint. Discussion started: 8 February 2023

(27.83°-28.17°N, 86.75° - 87°E)	-0.35 ± 0.12	2001 - 2018	
Everest area (27.83°-28.17°N, 86.75° - 87°E)	-0.32 ± 0.08	1970 - 2007	Bolch et al. (2011)*

* By using the Corona KH-4

Table A4 Statistics for the mass balance from Shean's and Brun's Study. The units of mass balance (MB) and uncertainties are m w.e. yr^{-1}

Region	This study (1970s-2000)		Shean's (2000-2018)		Brun's (2000-2016)		Average (Shean & Brun's)	
	MB	Error	MB	Error	MB	Error	MB	Error
Ganges	-0.28	0.18	-0.34	0.27	-0.31	0.44	-0.33	0.36
Brahmaputra	-0.27	0.12	-0.42	0.37	-0.43	0.46	-0.42	0.41
Salween	-0.32	0.10	-0.52	0.30	-0.63	0.49	-0.57	0.40
Yellow	-0.20	0.18	-0.46	0.26	—	—	-0.46	0.26
Yangtze	-0.25	0.15	-0.40	0.27	-0.35	0.33	-0.37	0.30
Mekong	-0.29	0.13	-0.45	0.31	-0.49	0.41	-0.47	0.36
Irrawaddy	-0.19	0.37	-0.59	0.44	-0.48	0.57	-0.53	0.50

Author contributions. SL designed the framework of the mass change database. YZ programmed the co-registration algorithms, produced the two mass change datasets, and wrote the manuscript. SL edited the first manuscript. TB reviewed and improved the manuscript. JW, KW, JX, WG, ZJ, FX, YY, DS, XY and ZZ adjusted and transformed the digitized contour maps and produced the Topo DEM. All authors discussed and improved the manuscript.

Acknowledgments. We thank the Chinese Military Geodetic Service for providing the digitized contour maps.

Financial support. This research has been supported by the National Natural Science Foundation of China (Grant No. 42171129), the Research Project of Postdoctoral Research Fund of Yunnan Province (Grant No. C615300504038), the International Science and Technology Innovation Cooperation Program of the State Key Research and Development Program (Grant No. 2021YFE0116800), the Open Foundation from National Cryosphere Desert Data Center (Grant No.2021KF01), the Second Tibetan Plateau Scientific Expedition and Research program (Grant No. 2019QZKK0208), the Scientific Research Fund Project of Yunnan Education Department (Grant No.2022Y059).

References

Bamber, J. L. and Rivera, A.: A review of remote sensing methods for glacier mass balance determination, Global and Planetary Change, 59, 138-148, https://doi.org/10.1016/j.gloplacha.2006.11.031, 2007.

Berthier, E., Arnaud, Y., Vincent, C., and Rémy, F.: Biases of SRTM in high-mountain areas: Implications for the monitoring of glacier volume changes, Geophysical Research Letters, 33, https://doi.org/10.1029/2006gl025862, 2006.

Berthier, E., Cabot, V., Vincent, C., and Six, D.: Decadal Region-Wide and Glacier-Wide Mass Balances Derived from Multi-Temporal ASTER Satellite Digital Elevation Models. Validation over the Mont-Blanc Area, Frontiers in Earth Science, 4, 63, https://doi.org/10.3389/feart.2016.00063, 2016.

Berthier, E., Arnaud, Y., Kumar, R., Ahmad, S., Wagnon, P., and Chevallier, P.: Remote sensing estimates of glacier mass balances in the Himachal Pradesh (Western Himalaya, India), Remote Sensing of Environment, 108, 327-338, https://doi.org/10.1016/j.rse.2006.11.017, 2007.

Bhattacharya, A., Bolch, T., Mukherjee, K., Pieczonka, T., KropÁČEk, J. A. N., and Buchroithner, M. F.: Overall recession and mass budget of Gangotri Glacier, Garhwal Himalayas, from 1965 to 2015 using remote sensing data, Journal of

https://doi.org/10.5194/essd-2022-473
Preprint. Discussion started: 8 February 2023

Glaciology, 62, 1115-1133, https://doi.org/10.1017/jog.2016.96, 2016.

Bhattacharya, A., Bolch, T., Mukherjee, K., King, O., Menounos, B., Kapitsa, V., Neckel, N., Yang, W., and Yao, T.: High Mountain Asian glacier response to climate revealed by multi-temporal satellite observations since the 1960s, Nat Commun, 12, 4133, https://doi.org/10.1038/s41467-021-24180-y, 2021.

Bolch, T.: Past and Future Glacier Changes in the Indus River Basin, in: Indus River Basin, 85-97, https://doi.org/10.1016/b978-0-12-812782-7.00004-7, 2019.

Bolch, T., Pieczonka, T., and Benn, D. I.: Multi-decadal mass loss of glaciers in the Everest area (Nepal Himalaya) derived from stereo imagery, The Cryosphere, 5, 349-358, https://doi.org/10.5194/tc-5-349-2011, 2011.

Bolch, T., Kulkarni, A., Kaab, A., Huggel, C., Paul, F., Cogley, J. G., Frey, H., Kargel, J. S., Fujita, K., Scheel, M., Bajracharya, S., and Stoffel, M.: The state and fate of Himalayan glaciers, Science, 336, 310-314, https://doi.org/10.1126/science.1215828, 2012.

Brun, F., Berthier, E., Wagnon, P., Kaab, A., and Treichler, D.: A spatially resolved estimate of High Mountain Asia glacier mass balances, 2000-2016, Nat Geosci, 10, 668-673, https://doi.org/10.1038/NGEO2999, 2017.

Brunt, K. M., Neumann, T. A., and Smith, B. E.: Assessment of ICESat-2 Ice Sheet Surface Heights, Based on Comparisons Over the Interior of the Antarctic Ice Sheet, Geophysical Research Letters, 46, 13072-13078, https://doi.org/10.1029/2019gl084886, 2019.

Carabajal, C. C. and Harding, D. J.: SRTM C-Band and ICESat Laser Altimetry Elevation Comparisons as a Function of Tree Cover and Relief, Photogrammetric Engineering & Remote Sensing, 72, 287-298, https://doi.org/10.14358/pers.72.3.287, 2006.

Curlander, J. C. and Mcdonough, R. N.: Synthetic Aperture Radar: Systems and Signal Processing, John Wiley & Sons, 1991.

Dehecq, A., Millan, R., Berthier, E., Gourmelen, N., Trouve, E., and Vionnet, V.: Elevation Changes Inferred From TanDEM-X Data Over the Mont-Blanc Area: Impact of the X-Band Interferometric Bias, Ieee J-Stars, 9, 3870-3882, https://doi.org/10.1109/jstars.2016.2581482, 2016.

Dehecq, A., Gourmelen, N., Gardner, A. S., Brun, F., Goldberg, D., Nienow, P. W., Berthier, E., Vincent, C., Wagnon, P., and Trouvé, E.: Twenty-first century glacier slowdown driven by mass loss in High Mountain Asia, Nature Geoscience, 12, 22-27, https://doi.org/10.1038/s41561-018-0271-9, 2018.

Farr, T. G., Rosen, P. A., Caro, E., Crippen, R., Duren, R., Hensley, S., Kobrick, M., Paller, M., Rodriguez, E., Roth, L., Seal, D., Shaffer, S., Shimada, J., Umland, J., Werner, M., Oskin, M., Burbank, D., and Alsdorf, D.: The Shuttle Radar Topography Mission, Reviews of Geophysics, 45, https://doi.org/10.1029/2005rg000183, 2007.

Gardelle, J., Berthier, E., Arnaud, Y., and Kääb, A.: Region-wide glacier mass balances over the Pamir-Karakoram-Himalaya during 1999-2011, The Cryosphere, 7, 1263-1286, https://doi.org/10.5194/tc-7-1263-2013, 2013.

Habib, M.: Evaluation of DEM interpolation techniques for characterizing terrain roughness, Catena, 198, https://doi.org/10.1016/j.catena.2020.105072, 2021.

Harrison, W. D.: How do glaciers respond to climate? Perspectives from the simplest models, Journal of Glaciology, 59, 949-960, https://doi.org/10.3189/2013JoG13J048, 2013.

Hewitt, K.: Glacier Change, Concentration, and Elevation Effects in the Karakoram Himalaya, Upper Indus Basin, Mountain Research and Development, 31, 188-200, https://doi.org/10.1659/mrd-journal-d-11-00020.1, 2011.

Hoelzle, M., Haeberli, W., Dischl, M., and Peschke, W.: Secular glacier mass balances derived from cumulative glacier length changes, Global and Planetary Change, 36, 295-306, https://doi.org/10.1016/s0921-8181(02)00223-0, 2003.

Hoffmann, J. R. and Walter, D.: How complementary are SRTM-X and -C band digital elevation models?, Photogrammetric Engineering and Remote Sensing, 72, 261-268, https://doi.org/10.14358/PERS.72.3.261, 2006.

Hugonnet, R., McNabb, R., Berthier, E., Menounos, B., Nuth, C., Girod, L., Farinotti, D., Huss, M., Dussaillant, I., Brun, F., and Kaab, A.: Accelerated global glacier mass loss in the early twenty-first century, Nature, 592, 726-731,

https://doi.org/10.5194/essd-2022-473
Preprint. Discussion started: 8 February 2023

https://doi.org/10.1038/s41586-021-03436-z, 2021.

Huss, M.: Density assumptions for converting geodetic glacier volume change to mass change, The Cryosphere, 7, 877-887, https://doi.org/10.5194/tc-7-877-2013, 2013.

Immerzeel, W. W., Pellicciotti, F., and Bierkens, M. F. P.: Rising river flows throughout the twenty-first century in two Himalayan glacierized watersheds, Nature Geoscience, 6, 742-745, https://doi.org/10.1038/ngeo1896, 2013.

Immerzeel, W. W., van Beek, L. P., and Bierkens, M. F.: Climate change will affect the Asian water towers, Science, 328, 1382-1385, https://doi.org/10.1126/science.1183188, 2010.

Immerzeel, W. W., Lutz, A. F., Andrade, M., Bahl, A., Biemans, H., Bolch, T., Hyde, S., Brumby, S., Davies, B. J., Elmore, A. C., Emmer, A., Feng, M., Fernandez, A., Haritashya, U., Kargel, J. S., Koppes, M., Kraaijenbrink, P. D. A., Kulkarni, A. V., Mayewski, P. A., Nepal, S., Pacheco, P., Painter, T. H., Pellicciotti, F., Rajaram, H., Rupper, S., Sinisalo, A., Shrestha, A. B., Viviroli, D., Wada, Y., Xiao, C., Yao, T., and Baillie, J. E. M.: Importance and vulnerability of the world's water towers, Nature, 577, 364-369, https://doi.org/10.1038/s41586-019-1822-y, 2020.

Junfeng, W., Shiyin, L., Wanqin, G., Junli, X., Weijia, B., and Donghui, S.: Changes in Glacier Volume in the North Bank of the Bangong Co Basin from 1968 to 2007 Based on Historical Topographic Maps, SRTM, and ASTER Stereo Images, Arctic, Antarctic, and Alpine Research, 47, 301-311, https://doi.org/10.1657/aaar00c-13-129, 2018.

Kääb, A.: Glacier Volume Changes Using ASTER Satellite Stereo and ICESat GLAS Laser Altimetry. A Test Study on EdgeØya, Eastern Svalbard, IEEE Transactions on Geoscience and Remote Sensing, 46, 2823-2830, https://doi.org/10.1109/tgrs.2008.2000627, 2008.

Kääb, A., Treichler, D., Nuth, C., and Berthier, E.: Brief Communication: Contending estimates of 2003–2008 glacier mass balance over the Pamir–Karakoram–Himalaya, The Cryosphere, 9, 557-564, https://doi.org/10.5194/tc-9-557-2015, 2015.

Kääb, A., Berthier, E., Nuth, C., Gardelle, J., and Arnaud, Y.: Contrasting patterns of early twenty-first-century glacier mass change in the Himalayas, Nature, 488, 495-498, https://doi.org/10.1038/nature11324, 2012.

King, O., Bhattacharya, A., Bhambri, R., and Bolch, T.: Glacial lakes exacerbate Himalayan glacier mass loss, Sci Rep, 9, 18145, https://doi.org/10.1038/s41598-019-53733-x, 2019.

King, O., Bhattacharya, A., Ghuffar, S., Tait, A., Guilford, S., Elmore, A. C., and Bolch, T.: Six Decades of Glacier Mass Changes around Mt. Everest Are Revealed by Historical and Contemporary Images, One Earth, 3, 608-620, https://doi.org/10.1016/j.oneear.2020.10.019, 2020.

Kocak, Güven, Buyuksalih, G., and Jacobsen, K.: Analysis of digital elevation models determined by high resolution space images, Int. Arch. of Photogrammetry & Remote Sensing, Istanbul, Turkey2004.

Kumar, A., Negi, H. S., and Kumar, K.: Long-term mass balance modelling (1986-2018) and climate sensitivity of Siachen Glacier, East Karakoram, Environ Monit Assess, 192, 368, https://doi.org/10.1007/s10661-020-08323-0, 2020.

Liu, L., Jiang, L., Jiang, H., Wang, H., Ma, N., and Xu, H.: Accelerated glacier mass loss (2011–2016) over the Puruogangri ice field in the inner Tibetan Plateau revealed by bistatic InSAR measurements, Remote Sensing of Environment, 231, https://doi.org/10.1016/j.rse.2019.111241, 2019.

Liu, S., Zhu, Y., Wei, J., Wu, K., Xu, J., Guo, W., Jiang, Z., Xie, F., Yi, Y., Shangguan, D., Yao, X., and Zhang, Z.: Glacier-level and gridded mass change in the source rivers in the eastern Tibetan Plateau (1970s-2000), National Tibetan Plateau/Third Pole Environment Data Center [dataset], https://doi.org/10.11888/Cryos.tpdc.272884, 2022.

Markus, T., Neumann, T., Martino, A., Abdalati, W., Brunt, K., Csatho, B., Farrell, S., Fricker, H., Gardner, A., Harding, D., Jasinski, M., Kwok, R., Magruder, L., Lubin, D., Luthcke, S., Morison, J., Nelson, R., Neuenschwander, A., Palm, S., Popescu, S., Shum, C. K., Schutz, B. E., Smith, B., Yang, Y., and Zwally, J.: The Ice, Cloud, and land Elevation Satellite-2 (ICESat-2): Science requirements, concept, and implementation, Remote Sensing of Environment, 190, 260-273, https://doi.org/10.1016/j.rse.2016.12.029, 2017.

Maurer, J., Schaefer, J., Rupper, S., and Corley, A.: Acceleration of ice loss across the Himalayas over the past 40 years,

https://doi.org/10.5194/essd-2022-473
Preprint. Discussion started: 8 February 2023

Science Advances, 5, eaav7266, https://doi.org/10.1126/sciadv.aav7266, 2019.

Maurer, J. M., Rupper, S. B., and Schaefer, J. M.: Quantifying ice loss in the eastern Himalayas since 1974 using declassified spy satellite imagery, The Cryosphere, 10, 2203-2215, https://doi.org/10.5194/tc-10-2203-2016, 2016.

Nuth, C. and Kääb, A.: Co-registration and bias corrections of satellite elevation data sets for quantifying glacier thickness change, The Cryosphere, 5, 271-290, https://doi.org/10.5194/tc-5-271-2011, 2011.

Paul, F.: Calculation of glacier elevation changes with SRTM: is there an elevation-dependent bias?, Journal of Glaciology, 54, 945-946, https://doi.org/10.3189/002214308787779960, 2008.

Pfeffer, W. T., Arendt, A. A., Bliss, A., Bolch, T., Cogley, J. G., Gardner, A. S., Hagen, J.-O., Hock, R., Kaser, G., Kienholz, C., Miles, E. S., Moholdt, G., Mölg, N., Paul, F., Radić, V., Rastner, P., Raup, B. H., Rich, J., and Sharp, M. J.: The Randolph Glacier Inventory: a globally complete inventory of glaciers, Journal of Glaciology, 60, 537-552, https://doi.org/10.3189/2014JoG13J176, 2014.

Pieczonka, T. and Bolch, T.: Region-wide glacier mass budgets and area changes for the Central Tien Shan between ~1975 and 1999 using Hexagon KH-9 imagery, Global and Planetary Change, 128, 1-13, https://doi.org/10.1016/j.gloplacha.2014.11.014, 2015.

Pieczonka, T., Bolch, T., and Buchroithner, M.: Generation and evaluation of multitemporal digital terrain models of the Mt. Everest area from different optical sensors, ISPRS Journal of Photogrammetry and Remote Sensing, 66, 927-940, https://doi.org/10.1016/j.isprsjprs.2011.07.003, 2011.

Pieczonka, T., Bolch, T., Junfeng, W., and Shiyin, L.: Heterogeneous mass loss of glaciers in the Aksu-Tarim Catchment (Central Tien Shan) revealed by 1976 KH-9 Hexagon and 2009 SPOT-5 stereo imagery, Remote Sensing of Environment, 130, 233-244, https://doi.org/10.1016/j.rse.2012.11.020, 2013.

Ragettli, S., Bolch, T., and Pellicciotti, F.: Heterogeneous glacier thinning patterns over the last 40 years in Langtang Himal, Nepal, The Cryosphere, 10, 2075-2097, https://doi.org/10.5194/tc-10-2075-2016, 2016.

Rignot, E., Echelmeyer, K., and Krabill, W.: Penetration depth of interferometric synthetic-aperture radar signals in snow and ice, Geophysical Research Letters, 28, 3501-3504, https://doi.org/10.1029/2000gl012484, 2001.

Rodríguez, E., Morris, C. S., and Belz, J. E.: A Global Assessment of the SRTM Performance, Photogrammetric Engineering and Remote Sensing, 72, 249-260, https://doi.org/10.14358/PERS.72.3.249, 2006.

Sakai, A., Nuimura, T., Fujita, K., Takenaka, S., Nagai, H., and Lamsal, D.: Climate regime of Asian glaciers revealed by GAMDAM glacier inventory, The Cryosphere, 9, 865-880, https://doi.org/10.5194/tc-9-865-2015, 2015.

Scherler, D., Bookhagen, B., and Strecker, M. R.: Spatially variable response of Himalayan glaciers to climate change affected by debris cover, Nature Geoscience, 4, 156-159, https://doi.org/10.1038/ngeo1068, 2011.

Shean, D. E., Bhushan, S., Montesano, P., Rounce, D. R., Arendt, A., and Osmanoglu, B.: A Systematic, Regional Assessment of High Mountain Asia Glacier Mass Balance, Frontiers in Earth Science, 7, https://doi.org/10.3389/feart.2019.00363, 2020.

Shi, Y.: Concise Glacier Inventory of China, Shanghai Science Spreading Publishing House, Shanghai2008.

Shi, Y., Huang, M., and Ren, B.: An Introduction to the Glaciers in China, Science Press, Beijing, 50-90 pp.1988.

Siebert, S., Kummu, M., Porkka, M., Döll, P., Ramankutty, N., and Scanlon, B. R.: A global data set of the extent of irrigated land from 1900 to 2005, Hydrology and Earth System Sciences, 19, 1521-1545, https://doi.org/10.5194/hess-19-1521-2015, 2015.

Smith, B., H. A. Fricker, A. Gardner, M. R. Siegfried, S. Adusumilli, B. M. Csathó, N. H., J. Nilsson, F. S. P., and Team, t. I.-S.: ATLAS/ICESat-2 L3A Land Ice Height (3rd) [dataset], https://doi.org/10.5067/ATLAS/ATL06.003, 2020.

Smith, B., Fricker, H. A., Holschuh, N., Gardner, A. S., Adusumilli, S., Brunt, K. M., Csatho, B., Harbeck, K., Huth, A., Neumann, T., Nilsson, J., and Siegfried, M. R.: Land ice height-retrieval algorithm for NASA's ICESat-2 photon-counting laser altimeter, Remote Sensing of Environment, 233, https://doi.org/10.1016/j.rse.2019.111352, 2019.

Wang, R., Liu, S., Shangguan, D., Radić, V., and Zhang, Y.: Spatial Heterogeneity in Glacier Mass-Balance Sensitivity

https://doi.org/10.5194/essd-2022-473
Preprint. Discussion started: 8 February 2023

710 across High Mountain Asia, Water, 11, https://doi.org/10.3390/w11040776, 2019.

Watson, C. S., Quincey, D. J., Carrivick, J. L., Smith, M. W., Rowan, A. V., and Richardson, R.: Heterogeneous water storage and thermal regime of supraglacial ponds on debris-covered glaciers, Earth Surface Processes and Landforms, 43, 229-241, https://doi.org/10.1002/esp.4236, 2018.

Wu, K., Liu, S., Zhu, Y., Liu, Q., and Jiang, Z.: Dynamics of glacier surface velocity and ice thickness for maritime 715 glaciers in the southeastern Tibetan Plateau, Journal of Hydrology, 590, https://doi.org/10.1016/j.jhydrol.2020.125527, 2020.

Wu, K., Liu, S., Jiang, Z., Xu, J., Wei, J., and Guo, W.: Recent glacier mass balance and area changes in the Kangri Karpo Mountains from DEMs and glacier inventories, The Cryosphere, 12, 103-121, https://doi.org/10.5194/tc-12-103-2018, 2018.

720 Xu, J., Shangguan, D., and Wang, J.: Three-Dimensional Glacier Changes in Geladandong Peak Region in the Central Tibetan Plateau, Water, 10, 1749, https://doi.org/10.3390/w10121749, 2018.

Ye, Q., Zong, J., Tian, L., Cogley, J. G., Song, C., and Guo, W.: Glacier changes on the Tibetan Plateau derived from Landsat imagery: mid-1970s – 2000–13, Journal of Glaciology, 63, 273-287, https://doi.org/10.1017/jog.2016.137, 2017.

Ye, Q., Bolch, T., Naruse, R., Wang, Y., Zong, J., Wang, Z., Zhao, R., Yang, D., and Kang, S.: Glacier mass changes in 725 Rongbuk catchment on Mt. Qomolangma from 1974 to 2006 based on topographic maps and ALOS PRISM data, Journal of Hydrology, 530, 273-280, https://doi.org/10.1016/j.jhydrol.2015.09.014, 2015.

Zemp, M., Thibert, E., Huss, M., Stumm, D., Rolstad Denby, C., Nuth, C., Nussbaumer, S. U., Moholdt, G., Mercer, A., Mayer, C., Joerg, P. C., Jansson, P., Hynek, B., Fischer, A., Escher-Vetter, H., Elvehøy, H., and Andreassen, L. M.: Reanalysing glacier mass balance measurement series, The Cryosphere, 7, 1227-1245, https://doi.org/10.5194/tc-7-1227-730 2013, 2013.

Zhang, Y., Hirabayashi, Y., and Liu, S.: Catchment-scale reconstruction of glacier mass balance using observations and global climate data: Case study of the Hailuogou catchment, south-eastern Tibetan Plateau, Journal of Hydrology, 444-445, 146-160, https://doi.org/10.1016/j.jhydrol.2012.04.014, 2012.

Zhao, F., Long, D., Li, X., Huang, Q., and Han, P.: Rapid glacier mass loss in the Southeastern Tibetan Plateau since the 735 year 2000 from satellite observations, Remote Sensing of Environment, 270, https://doi.org/10.1016/j.rse.2021.112853, 2022.

Zhou, Y., Li, Z., Li, J., Zhao, R., and Ding, X.: Glacier mass balance in the Qinghai–Tibet Plateau and its surroundings from the mid-1970s to 2000 based on Hexagon KH-9 and SRTM DEMs, Remote Sensing of Environment, 210, 96-112, https://doi.org/10.1016/j.rse.2018.03.020, 2018.

740